UC Berkeley
UC Berkeley Previously Published Works

Title
Nonlinear optical selection rule based on valley-exciton locking in monolayer ws(2)

Permalink
https://escholarship.org/uc/item/7788025c

Journal
LIGHT-SCIENCE & APPLICATIONS, 4(12)

ISSN
2047-7538

Authors
Xiao, Jun
Ye, Ziliang
Wang, Ying
et al.

Publication Date
2015-12-01

DOI
10.1038/lsa.2015.139

Peer reviewed

eScholarship.org Powered by the California Digital Library
University of California

OPEN

Light: Science & Applications (2015) 4, e366; doi:10.1038/lsa.2015.139
© 2015 CIOMP. All rights reserved 2047-7538/15
www.nature.com/lsa

ORIGINAL ARTICLE

Nonlinear optical selection rule based on valley-exciton locking in monolayer ws_2

Jun Xiao[1], Ziliang Ye[1], Ying Wang[1], Hanyu Zhu[1], Yuan Wang[1,2] and Xiang Zhang[1,2,3]

Optical selection rules fundamentally determine the optical transitions between energy states in a variety of physical systems, from hydrogen atoms to bulk crystals such as gallium arsenide. These rules are important for optoelectronic applications such as lasers, energy-dispersive X-ray spectroscopy, and quantum computation. Recently, single-layer transition metal dichalcogenides have been found to exhibit valleys in momentum space with nontrivial Berry curvature and excitons with large binding energy. However, there has been little study of how the unique valley degree of freedom combined with the strong excitonic effect influences the nonlinear optical excitation. Here, we report the discovery of nonlinear optical selection rules in monolayer WS_2, an important candidate for visible 2D optoelectronics because of its high quantum yield and large direct bandgap. We experimentally demonstrated this principle for second-harmonic generation and two-photon luminescence (TPL). Moreover, the circularly polarized TPL and the study of its dynamics evince a sub-ps interexciton relaxation ($2p \rightarrow 1s$). The discovery of this new optical selection rule in a valleytronic 2D system not only considerably enhances knowledge in this area but also establishes a foundation for the control of optical transitions that will be crucial for valley optoelectronic device applications such as 2D valley-polarized THz sources with $2p$–$1s$ transitions, optical switches, and coherent control for quantum computing.
Light: Science & Applications (2015) **4,** e366; doi:10.1038/lsa.2015.139; published online 18 December 2015

Keywords: nonlinear optical selection rule; 2D materials; $2p$–$1s$ exciton relaxation; valley exciton

INTRODUCTION

An optical selection rule is a fundamental principle dictating allowed and forbidden transitions. It is strictly imposed by various symmetries, such as temporal translational, spatial translational, and rotational symmetry, and their corresponding laws of conservation of energy, momentum, and angular momentum according to Noether's theorem. In particular, the angular momentum contributed by an electron's orbit and spin is important for revealing the symmetry of electronic states in atoms using atomic emission spectroscopy, controlling the polarization of semiconductor light-emitting diodes and lasers, and optically manipulating spin polarization in spintronics[1,2]. In conventional selection rule studies of solids such as bulk gallium arsenide and their quantum wells, the angular momenta of Bloch electrons are believed to be inherited exclusively from their atomic orbits[3]. Because of the requirement of inversion symmetry breaking and optical transitions off the center of the Brillouin zone[4], the role of intercellular electron motion in selection rules received little attention until the recent discovery of valley angular momentum (VAM) in transition metal dichalcogenide (TMDC) monolayers, which have a direct bandgap at the edge of the Brillouin zone and lack inversion symmetry[5–8].

The VAM is associated with energy valleys in momentum space in TMDC monolayers. The inversion symmetry breaking makes it possible for the VAM of Bloch electrons to include contributions from not only individual atomic orbits but also the circulation of electrons from one atomic site to another throughout the crystal unit cell. Bloch electrons in adjacent valleys have VAMs with opposite signs and follow a valley-dependent optical selection rule in the linear spectrum[5–7]. Recent studies have reported that monolayer WS_2 exhibits a strong excitonic effect due to reduced dielectric screening[9–15]. The high quantum yield and large direct bandgap of WS_2 are also important for future 2D optoelectronics in the visible range[16]. Similar to the hydrogen atom, an exciton confined in a 2D plane also possesses an excitonic angular momentum (EAM) resulting from the orbital motion of the electron relative to the hole. Although valley-dependent second-harmonic generation (SHG) and two-photon luminescence (TPL) in the near-infrared region have been recently observed in monolayer WSe_2[17,18], direct observations of how the EAM and VAM determine nonlinear optical processes in the visible range are still lacking. Here, we report nonlinear optical selection rules based on the valley-exciton locked relationship imposed by the EAM and VAM combined in monolayer WS_2. In addition, we studied the TPL dynamics in TMDC monolayers for the first time and demonstrated a sub-ps $2p$–$1s$ exciton relaxation involving phonons. These new selection rules and interexciton relaxation ($2p$–$1s$) in this 2D system not only are of fundamental importance in determining optical transitions and encoding information in valleytronics[19] with multiple excitonic degrees but also provide important guidance for the design of future 2D THz sources and optical switches.

[1]NSF Nanoscale Science and Engineering Center (NSEC), University of California at Berkeley, Berkeley, CA, USA; [2]Material Sciences Division, Lawrence Berkeley National Laboratory, Berkeley, CA, USA and [3]Department of Physics, King Abdulaziz University, Jeddah, Saudi Arabia
Correspondence: X Zhang, Email: xiang@berkeley.edu
Received 14 August 2015; revised 3 September 2015; accepted 5 September 2015; accepted article preview online 6 September 2015

MATERIALS AND METHODS

Monolayer WS_2 samples were mechanically exfoliated onto 275 nm SiO_2/Si substrates from chemical vapor transport synthetic crystal flakes (2D Semiconductors Inc., Scottsdale, USA). The exfoliated monolayers were typically 5–10 micrometers in size and were characterized using tools such as atomic force microscopy and Raman and photoluminescence spectroscopy. The excitation light was extracted using an optical parametric oscillator (Inspire HF 100, Spectra Physics, Santa Clara, USA) pumped by a mode-locked Ti:sapphire oscillator. The laser pulse width was approximately 200 fs, and the repetition rate was 80 MHz. The excitation laser was linearly polarized by a 900–1300 nm polarizing beamsplitter. The transmitted p-polarized laser light was converted into circularly polarized light *via* a broadband Fresnel Rhomb quarter-wave retarder. The low-temperature experiment was performed in a continuous-flow liquid helium cryostat equipped with a 50× objective with a long working distance. The emission signal was detected in the backscattering configuration, analyzed using the Fresnel Rhomb quarter-wave retarder followed by a visible-range polarizer, and finally collected by a cooled CCD spectrometer. For time-resolved one-photon and two-photon photoluminescence spectroscopy, the signal passing through a bandpass filter with a bandwidth of 30 meV was collected by a Hamamatsu synchroscan streak camera with an overall time resolution of 2 ps. The transmissivity of the optical system was carefully calibrated to evaluate the absolute power level at the focusing plane. The emission spectra were normalized to the square of the focused power, as the excitation was limited to the unsaturated regime. The laser pulse width was measured using a home-built autocorrelator at the focus throughout the scanning range.

RESULTS AND DISCUSSION

The three-fold rotational symmetry in monolayer WS_2 requires total angular momentum conservation during light–matter interactions, in which the VAM, EAM, lattice angular momentum, and photon spin angular momentum are exchanged with each other. Induced by the local atomic orbital angular momentum and nontrivial Berry curvature distribution, the VAM has an out-of-plane component in both the conduction ($\tau\hbar = 1\hbar$ or $-1\hbar$ at K′ or K valleys, respectively) and valence ($\tau\hbar = 0\hbar$ at K′ or K valleys) bands. Meanwhile, the relative electron–hole motion is confined to a 2D plane, resulting in an exciton wavefunction in the form of $R_{n,l}(\rho)e^{il\varphi}$ with only an out-of-plane $l\hbar$ EAM, where φ is the azimuthal angle and ρ is the electron–hole distance[20,21]. The out-of-plane VAM and EAM are combined collinearly. In addition, the crystal transforms the impinging angular momentum into a modulus of three by absorbing the excess angular momentum into the lattice, in a manner similar to the Umklapp process in phonon scattering[22,23]. As a result, under normally incident light, the conservation of out-of-plane angular momentum yields the following optical selection rule for the unique VAM and EAM in monolayer WS_2:

$$\Delta m\hbar = \Delta\tau\hbar + \Delta l\hbar + 3N\hbar, (N \text{ is an integer}) \quad (1)$$

Upon absorption, the change in the spin angular momentum of the photons, $\Delta m\hbar$, results in changes in the angular momenta of the valley ($\Delta\tau\hbar$), exciton ($\Delta l\hbar$) and crystal lattice ($3N\hbar$). Although strong spin-orbit coupling is present, the spin of the electron does not flip under the dominant electric dipole transition. Therefore, the unchanged out-of-plane spin angular momentum makes no contribution to Equation (1).

Clearly, both the TPL and SHG processes exhibit a valley-exciton locked selection rule as described by Equation (1), meaning that excitonic resonant two-photon processes occur only within specific valleys under pure $\sigma+$, or $\sigma-$ excitation. For example, in the 1*s* resonant SHG process, the transition from the ground state to the 1*s* state at a K valley requires a $-1\hbar$ VAM change and a $0\hbar$ EAM change. According to Equation (1), this can occur only through the absorption of two pure $\sigma+$ fundamental photons with $2\hbar$ and the emission of the excess $3\hbar$ angular momentum into the crystal lattice. The virtual 1*s* exciton in the K valley immediately emits a $\sigma-$ second-harmonic (SH) photon (Figure 1a). Under time reversal, only $\sigma-$ fundamental photons can trigger the transition from the ground state to the 1*s* state at a K′ valley, leading to the emission of a $\sigma+$ SH photon in the resonant SHG process. Therefore, SHG emission always has the opposite helicity from that of the incident light. In regard to 2*p* resonant TPL, only the transition from the ground state to the $2p_+$ state with an EAM of $+1\hbar$ at a K′ valley is induced under pure $\sigma+$ excitation. In this transition, the required $+1\hbar$ VAM and $+1\hbar$ EAM changes can be satisfied only by the absorption of two $\sigma+$ fundamental photons without any lattice contribution. The 2*p* exciton from the above transition relaxes to the 1*s* state and finally emits a $\sigma+$ photon (Figure 1b). Again governed by Equation (1), in the case of $\sigma-$ excitation, only TPL in a K valley occurs under time reversal. In contrast to the SHG case, 2*p* resonant TPL emission always exhibits the same helicity as that of the incident light. In Table 1, we provide a complete summary of the allowed and forbidden TPL and SHG transitions from the ground state to excitonic states with a strong optical response under pure circularly polarized incident light. In the following, we report polarization-resolved SHG and TPL spectral experiments that were performed to confirm this valley-exciton locked selection rule.

WS_2 monolayer samples were mechanically exfoliated onto SiO_2/Si substrates (Supplementary Fig. S1). A typical light emission spectrum under excitation at 1090 nm (1.14 eV) and 20 K by an ultrafast laser is shown in Figure 1c. One emission peak, at 2.28 eV, is assigned to SHG. The other two peaks observed at 2.09 eV and 2.05 eV correspond to the neutral and charged exciton emissions. The charged exciton emission is dominant and was selected as our TPL signal. These excitonic emitted photon energies are nearly two times higher than that of the excitation photon, and therefore, they can originate only from two-photon absorption. This conclusion is further confirmed in the inset to Figure 1c. Both the TPL and the SHG exhibit a quadratic power dependence, indicating their two-photon nature.

According to Equation (1), SHG emissions carry the opposite helicity from that of the incident light, whereas TPL emissions display the same helicity. We first experimentally examined the optical selection rule for SHG. An excitation energy scan of the SHG signal (Figure 2a) revealed a resonance at 2.09 eV, indicating exciton-enhanced SHG due to the 1*s* state. The magnitude of the SHG signal at the 1*s* resonance is enhanced by nearly one order of magnitude compared with that under non-resonant excitation. We then measured the SHG under $\sigma+$ excitation (Figure 2b) at the 1*s* resonance. The SHG helicity, defined as $\frac{I(\sigma+)-I(\sigma-)}{I(\sigma+)+I(\sigma-)} \times 100\%$, was found to be -99% at an excitation energy of 1.045 eV. The negative sign here indicates that the SHG has the opposite circular polarization from that of the fundamental light. Determined by the selection rule, such a high helicity value is preserved because SHG is an instantaneous process and free of any intervalley scattering processes[24]. The observations of nearly 100% negative helicity and intensity resonance in SHG are well consistent with the proposed valley-exciton locked selection rule.

In contrast to the SHG selection rule at the 1*s* resonance, TPL displays a completely opposite valley-dependent selection rule at the 2*p* resonance. In an excitation energy scan (Figure 3a), a dominant resonance was observed at 1.13 eV, corresponding to the 2*p* excitonic peak.

doi:10.1038/lsa.2015.139

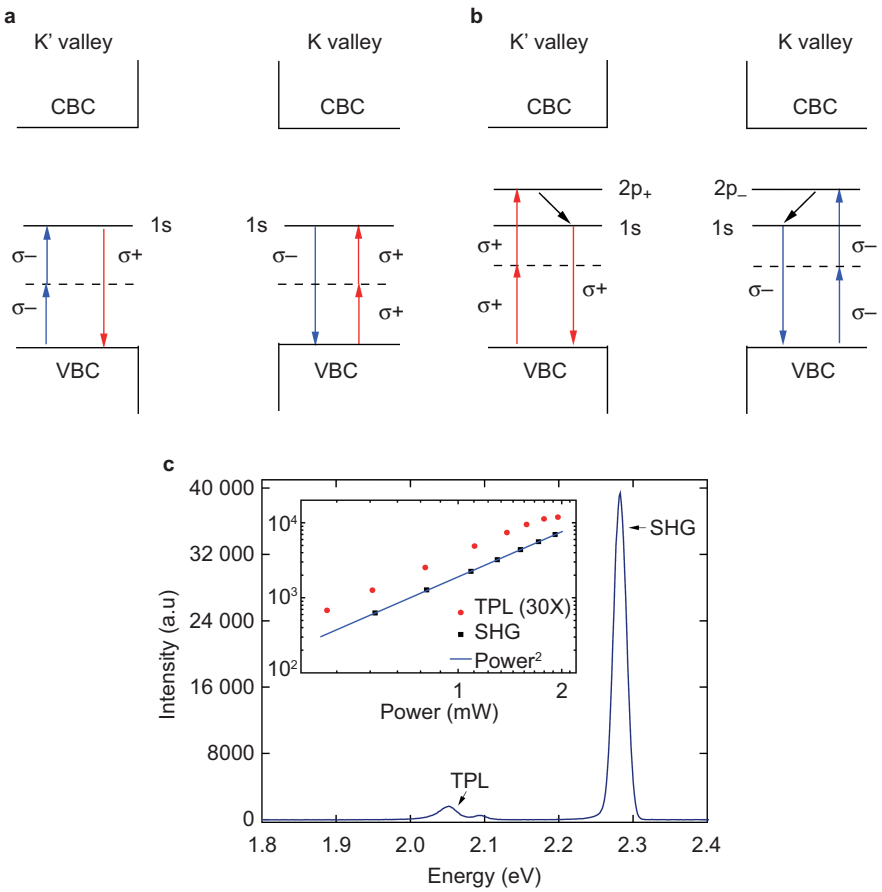

Figure 1 Schematic diagram of optical selection rules based on valley-exciton locking in 2D TMDC. (**a**) 1*s* exciton-resonant SHG in K′ and K valleys. Pumped by a σ+ (or σ−) polarized fundamental photon, an electron in the valence band at a K (or K′) valley reaches a virtual state. Within the lifetime of the virtual state, a second σ+ (or σ−) photon pumps the electron from the virtual state to the real 1*s* state in the K (or K′) valley. Immediately, a second-harmonic photon with a σ− (or σ+) polarization is emitted. (**b**) 2*p* exciton-resonant TPL in K′ and K valleys. Under two-photon excitation by σ+ (or σ−) polarized photons, the system transitions from the ground state to the real $2p_+$ (or $2p_-$) state with a change of $+1\hbar$ (or $-1\hbar$) in the EAM at a K′ (or K) valley through an intermediate virtual state. The 2*p* exciton relaxes to the 1*s* excitonic state and emits a σ+ (or σ−) photon. The conduction band continuum and valence band continuum are labeled as CBC and VBC, respectively. The solid lines represent real excitonic states, and the dashed lines represent virtual states. Red indicates σ+ polarization; blue indicates σ− polarization. (**c**) Typical emission spectrum of monolayer WS_2 pumped by a 1.14 eV laser pulse at 20 K. The peaks at 2.09 eV and 2.05 eV correspond to the 1*s* state of "A" neutral exciton and corresponding charged exciton (trion) created *via* TPL. The inversion symmetry breaking in monolayer WS_2 results in an SHG signal at 2.28 eV. In the inset, the power dependences of the TPL and SHG emissions are plotted, exhibiting quadratic behavior.

Table 1 Optical selection rules based on valley-exciton locking in 2D TMDC

	Δl	$\Delta\tau$	SHG	TPL
(1*s*, K)	0	−1	A/F	N/A
(1*s*, K′)	0	+1	F/A	N/A
($2p_+$, K)	+1	−1	F/F	F/F
($2p_+$, K′)	+1	+1	A/F	A/F
($2p_-$, K)	−1	−1	F/A	F/A
($2p_-$, K′)	−1	+1	F/F	F/F
(2*s*, K)	0	−1	A/F	N/A
(2*s*, K′)	0	+1	F/A	N/A

Resonant SHG and TPL are allowed only for excitonic states in specific valleys under pure σ+/σ− light excitation. $\Delta\tau\hbar$ and $\Delta l\hbar$ are the changes in VAM and EAM, respectively, from the ground state to resonant excitonic states. The change in the photon angular momentum is $2\hbar$ or $-2\hbar$ under pure σ+ or σ− illumination. The capital letters A and F indicate that the optical transition is "allowed" or "forbidden" under pure σ+/σ− illumination. N/A means "not available", indicating that the optical transition exhibits a negligible transition strength based on parity symmetry analysis. Red indicates σ+ emission; blue indicates σ− emission for either SHG or TPL.

Compared with the 1*s* excitonic level, the 2*p* exciton has a greater linewidth (~80 meV) and an asymmetric shape. To test the selection rule, we measured the TPL spectrum under σ+ light excitation (Figure 3b). The TPL helicity was measured to be 29.6% at the excitation energy (1.13 eV) and had the same sign as that of the incident light. The helicity changed sign when the monolayer was pumped with σ− light (see Supplementary Fig. S2). More interestingly, we observed a TPL resonance in the emission helicity at the 2*p* peak (Figure 3b inset), confirming our theory that the EAM imposes an additional selection rule on the optical transition. The relatively low helicity value observed here is due to the strong intervalley scattering upon the injection of such high energies[25]. Away from the 2*p* resonance peak, we always observed nonzero TPL with lower energy excitation, as shown in Figure 3a, indicating the presence of several non-excitonic states with *p* components below the 2*p* state. This background cannot originate from the re-absorption of the SHG emission because the emission helicity is positive.

Subsequently, we further examined the valley-exciton locked selection rule by performing time-resolved TPL measurements. After the initial two-photon absorption and the formation of 2*p* valley excitons,

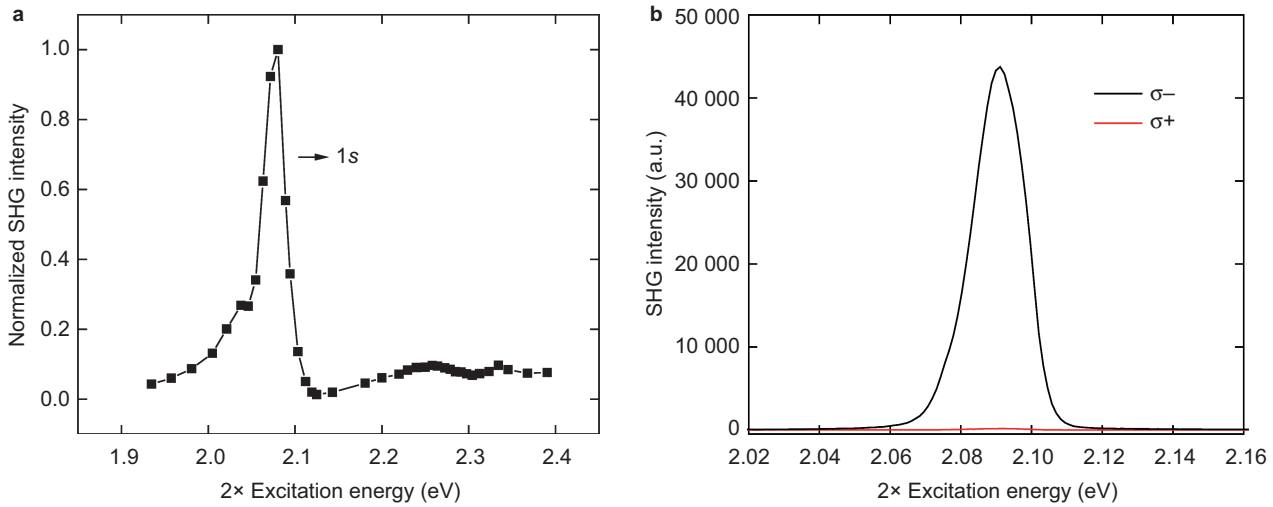

Figure 2 Experimental observation of the SHG selection rule in monolayer WS_2 at 20 K. (**a**) SHG intensity (black dots) versus SHG excitation energy in a scan from 0.97 eV to 1.19 eV. A dominant SHG intensity peak is observed at a pump energy of 1.045 eV, which is attributable to the 1*s* resonance. (**b**) Polarization-resolved SHG measurements for σ+ (red curve) and σ− (black curve) detection under pumping by σ+. A negative helicity of $P = -99.0\% \pm 0.1\%$ was observed from multiple repeated measurements. The excitation energy was 1.045 eV. The significant negative helicity at the 1*s* resonance confirms the existence of a rigorous selection rule for SHG.

two subsequent processes occur: the 2*p* excitons relax to 1*s* excitons, and these 1*s* excitons recombine. If the populations in the K and K′ valleys are unbalanced, intervalley scattering will occur. Here, we conducted time-resolved TPL measurements at the 2*p* resonance, and the signal was detected by a synchroscan streak camera with an overall time resolution of 2 ps. Under linearly polarized excitation light, the intervalley scattering has no net contribution because the populations in both types of valleys are equal. Therefore, the time-resolved TPL trace includes only relaxation and recombination (Figure 4a). The rising edge after excitation is predominantly associated with the relaxation process from 2*p* to 1*s*[26], whereas the recombination process is reflected by the decaying portion of the curve. To capture the essence of the dynamics, we used a three-level rate equation (Supplementary Information and Supplementary Fig. S3). Typically, a process no shorter than one tenth of the system's time resolution can be extracted by applying convolution fitting with the instrument response function (IRF)[27,28]. In this manner, we can infer that the interexciton relaxation time is $\tau_{2p-1s} = 600 \pm 150$ fs and that the recombination time is $\tau_{rec} = 5.0 \pm 0.2$ ps. Regarding the sub-ps 2*p*–1*s* relaxation, which is reported here in 2D TMDC for the first time, it was further verified by time-resolved PL measurements under near-resonance one-photon excitation (Figure 4b). The rising feature in this curve is much sharper compared with that under 2*p* resonant two-photon excitation, which indicates more rapid relaxation because of a smaller energy gap. Indeed, our fit shows that the relaxation time to the 1*s* exciton edge in this case is less than 200 fs (the fastest process can be extracted from convolution fitting). This confirms our observation of a measurable sub-ps 2*p*–1*s* relaxation due to the large energy gap between the 2*p* and 1*s* excitonic

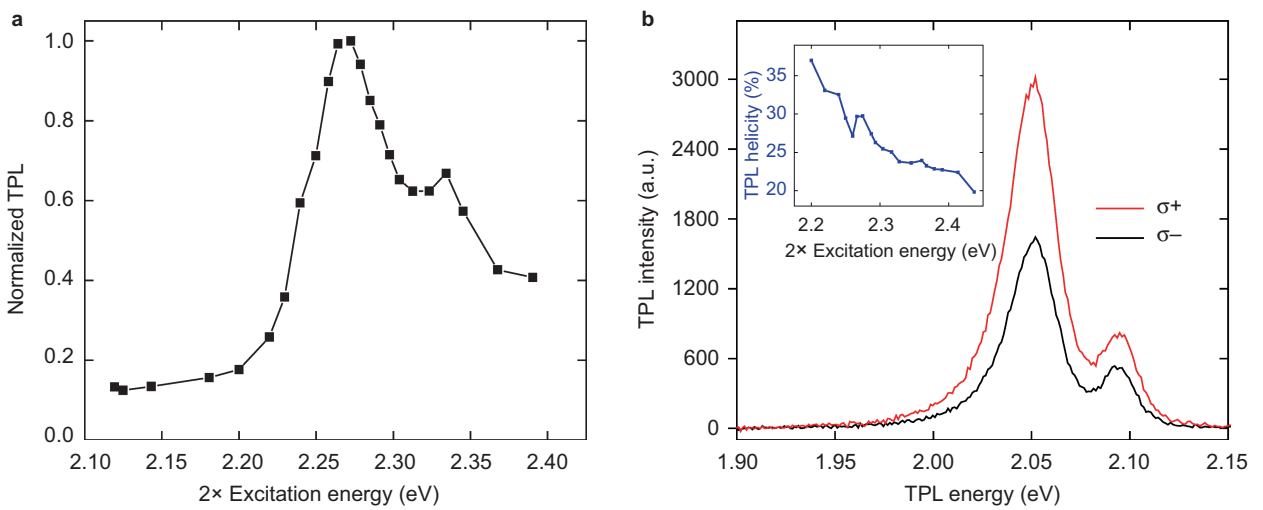

Figure 3 Experimental observation of the TPL selection rule in monolayer WS_2 at 20 K. (**a**) TPL intensity versus TPL excitation energy in a scan from 1.06 eV to 1.19 eV. A dominant TPL intensity peak resonance is observed under 1.13 eV laser pulse excitation, which is attributable to the 2*p* resonance. (**b**) Polarization-resolved TPL measurements for σ+ (red curve) and σ− (black curve) detection under σ+ light excitation. A circular polarization of $P = 29.6\% \pm 0.5\%$ was observed based on multiple repeated measurements. The excitation energy was 1.13 eV. The inset plots the TPL helicity versus the TPL excitation energy for a scan of the same range under excitation by σ+ polarized light. A helicity resonance is observed at the 2*p* excitonic level. Away from the 2*p* resonance, the TPL helicity decreases with increasing excitation energy due to the energy-dependent intervalley scattering.

doi:10.1038/lsa.2015.139

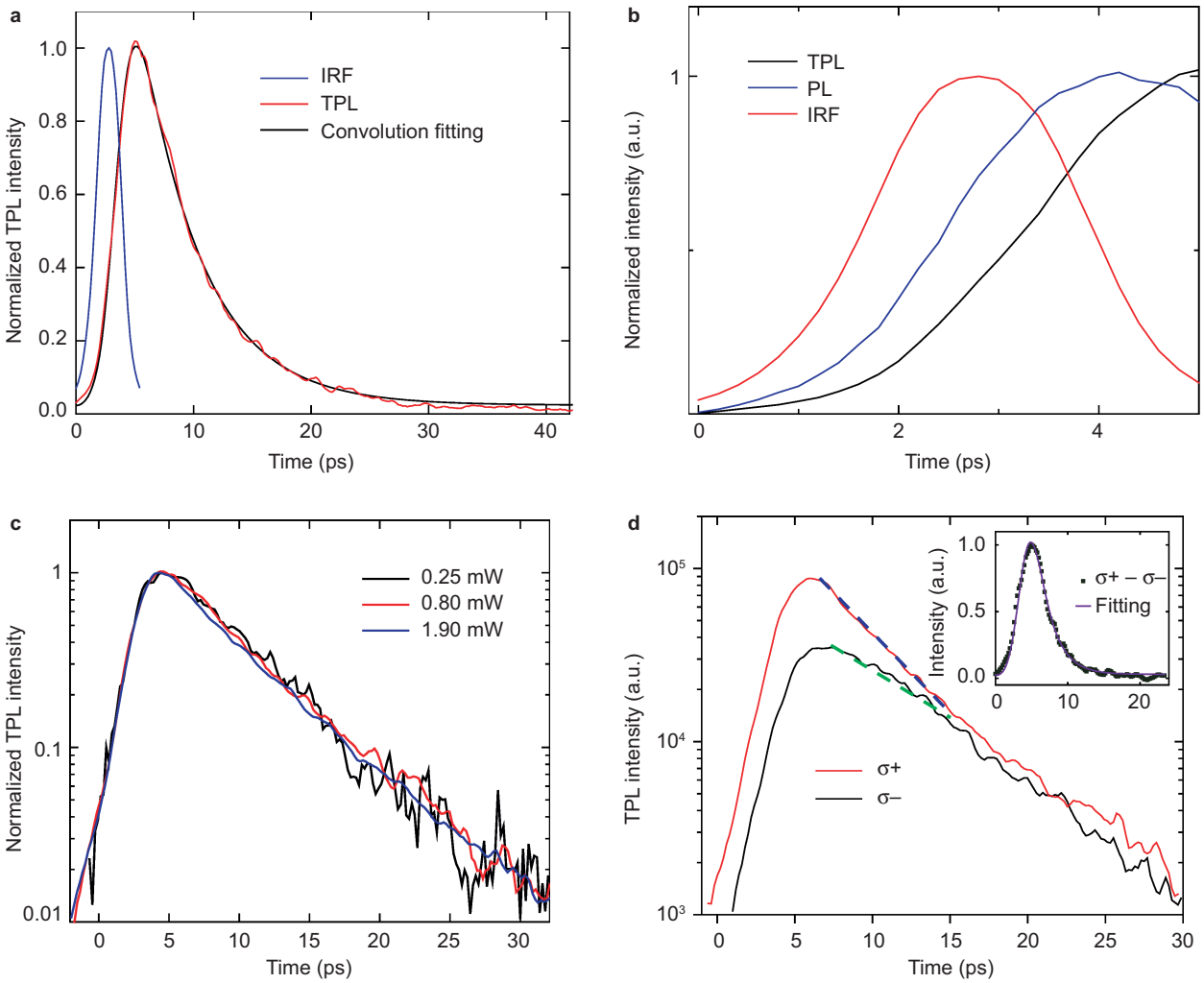

Figure 4 Time-resolved valley exciton dynamics in monolayer WS_2 at 20 K. (**a**) Time trace of the TPL (red curve) excited by a linearly polarized laser pulse at 1.13 eV. Compared with the instrument response function (IRF), presented as the blue curve, the TPL time trace exhibits observable rising and decaying features. Based on our three-level rate equation model (see the Supplementary Information), the results of convolution fitting (black curve) indicate an interexciton relaxation time τ_{2p-1s} of 600 ± 150 fs and a recombination time τ_{rec} of 5.0 ± 0.2 ps. (**b**) Relaxation dynamics comparison. The time-resolved relaxation curves (rising features) for two-photon-induced PL (TPL, black curve) and one-photon-induced PL (blue curve) are plotted. The one-photon-induced PL, excited near the resonance at 2.10 eV, exhibits a sharper rising feature compared with that of the TPL excited at the 2*p* resonance (2.26 eV). This difference confirms that the relaxation of the 2*p* exciton requires a longer time because of the larger energy gap. Here, the red curve represents the IRF. (**c**) Power-dependent time-resolved 2*p* resonant TPL. TPL time traces recorded under pumping by a laser pulse at 1.13 eV with different incident powers. The power was varied over one order of magnitude, resulting in a change in the exciton population of two orders of magnitude. No significant change in the dynamics is observed in this power range, thereby excluding exciton–exciton annihilation. (**d**) Polarization-resolved time traces of the TPL excited by σ+ polarized light at 1.13 eV. Because of the selection rule and intervalley scattering, the σ+ emission (red curve) displays a greater intensity and more rapid decay than does the σ− emission (black curve). The blue and green dashed lines are guides for the eye. The inset shows the convolution fit (purple curve) for the time-resolved valley exciton population (σ+ − σ−, black dots). The intervalley scattering times during relaxation, $\tau_{inter(2p-1s)}$, and recombination, $\tau_{inter(1s)}$, are estimated to be 3 ± 1 ps and 8.3 ± 0.5 ps. The error ranges were obtained from fitting to the results of multiple repeated measurements. PL, photoluminescence.

levels. Excited carrier relaxation can typically follow three possible pathways: carrier–carrier scattering, carrier–phonon scattering, and radiative emission. Carrier–carrier scattering is predominantly dependent on carrier density. However, as we varied the pump intensity, no significant change in the dynamics was observed (see Figure 4c). Therefore, carrier–carrier scattering is unlikely to account for the sub-ps relaxation here. Meanwhile, radiative emission from the 2*p*–1*s* transition can be excluded because the transition rate is not expected to be as fast as the sub-ps level. Given the comparable densities of states and transition matrix amplitudes calculated using the GW method[9,21], one should expect the 2*p*–1*s* transition time to be similar to the 1*s* exciton radiative lifetime. Because the radiative lifetime of the 1*s* exciton is approximately 100 ps in our case (the quantum yield is ~5%, and the lifetime of the nonradiative decay is 5 ps, as shown in Figure 4a), the sub-ps relaxation we observed cannot be radiative decay. Therefore, it is very likely to be attributable to exciton–phonon scattering. This is further confirmed by the broader linewidth of the 2*p* exciton (see Figure 3a). Under the assumption that the 2*p*–1*s* relaxation is accomplished *via* optical phonon cascade scattering, each phonon scattering event requires ~130 fs (the energy gap between the 2*p* and 1*s* levels is 220 meV, and the dominant optical phonons observed *via* Raman spectroscopy have energies of 44 meV for the E_{2g} mode and 51 meV for the A_{1g} mode). According to the uncertainty principle, this corresponds to an additional linewidth broadening of greater than 30 meV

compared with the 1*s* exciton. This is consistent with our observation, which indicates 40 meV of additional broadening. It is suspected that a 1*s* hot exciton with some kinetic energy is generated after a 2*p* exciton collides with a phonon and cascades to the 1*s* exciton edge. The rapid recombination observed at the 1*s* exciton edge ($\tau_{rec} = 5.0 \pm 0.2$ ps) is likely attributable to nonradiative recombination, such as defect trapping or a phonon-assisted process[29]. This is confirmed by the quantum yield measurement[18], which indicates a quantum yield of approximately 5%. We carefully checked that the nonradiative channel is not dependent on the excitation power (Figure 4c), which excludes any exciton–exciton annihilation mechanism[30].

For $\sigma+$ two-photon excitation at the 2*p* resonance, the dynamical curves for emission at the different polarizations are shown in Figure 4d. The $\sigma+$ TPL from the K′ valleys exhibits a higher intensity than that of the $\sigma-$ TPL from the K valleys, which again confirms the valley-exciton locked selection rule. Compared with the $\sigma+$ emission, the $\sigma-$ emission always undergoes slower decay until the populations in the two types of valleys are equal. This difference in the decay trend results from intervalley scattering, which tends to equalize the exciton populations in the two valleys. From convolution fitting with the IRF and recombination time, we can estimate the lifetimes of intervalley scattering during relaxation, $\tau_{inter(2p-1s)}$, and recombination, $\tau_{inter(1s)}$, to be 3 ± 1 ps and 8.3 ± 0.5 ps, respectively (Figure 4d inset). The exchange interaction between the electron and hole can induce both a spin flip and a momentum change *via* Coulomb potential scattering. Recent calculations show that this process can occur in the picosecond range and becomes more efficient when the exciton carries more energy[31], which may account for the rapid depolarization observed in our measurements.

CONCLUSION

In summary, we discovered nonlinear optical selection rules based on valley-exciton locking in monolayer WS_2. This important finding reveals that the EAM and VAM combined fundamentally determine the optical transitions in TMDC monolayers. These new selection rules together with the observed interexciton dynamics offer important guidance for the manipulation of exciton and valley degrees of freedom in 2D TMDC. For example, the well-defined excitonic levels located in distinguishable valleys could encode quantum information, potentially leading to the design of THz sources with 2*p*–1*s* transitions, optical switches and quantum interference control based on this 2D material[32–34].

AUTHORS' CONTRIBUTIONS

JX, YW, and HZ prepared the samples. JX performed the measurements. JX, ZY, YW, HZ and YW conducted the data analysis. XZ guided the research. All authors contributed to the preparation of the manuscript.

ACKNOWLEDGEMENTS

This work was supported by the "Light-Material Interactions in Energy Conversion" Energy Frontier Research Center funded by the U.S. Department of Energy, Office of Science, Office of Basic Energy Sciences under Award Number DE-AC02-05CH11231.

1 Hilton DJ, Tang CL. Optical orientation and femtosecond relaxation of spin-polarized hole in GaAs. *Phys Rev Lett* 2002; **89**: 146601.
2 Gerardot BD, Brunner D, Dalgarno PA, Öhberg P, Seidl S *et al*. Optical pumping of a single hole spin in a quantum dot. *Nature* 2008; **451**: 441–444.
3 Chuang SL. Physics of Photonic Devices. Hoboken, NJ: Wiley; 2009.
4 Yao W, Xiao D, Niu Q. Valley-dependent optoelectronics from inversion symmetry breaking. *Phys Rev B* 2008; **77**: 235406.
5 Mak KF, He K, Shan J, Heinz TF. Control of valley polarization in monolayer MoS_2 by optical helicity. *Nat Nanotechnol* 2012; **7**: 494–498.
6 Cao T, Wang G, Han WP, Ye HQ, Zhu CR *et al*. Valley-selective circular dichroism of monolayer molybdenum disulphide. *Nat Commun* 2012; **3**: 887.
7 Zeng HL, Dai JF, Yao W, Xiao D, Cui XD. Valley polarization in MoS_2 monolayers by optical pumping. *Nat Nanotechnol* 2012; **7**: 490–493.
8 Liu GB, Xiao D, Yao YG, Xu XD, Yao W. Electronic structures and theoretical modelling of two-dimensional group-VIB transition metal dichalcogenides. *Chem Soc Rev* 2015; **44**: 2643–2663.
9 Ye ZL, Cao T, O'Brien K, Zhu HY, Yin XB *et al*. Probing excitonic dark states in single-layer tungsten disulphide. *Nature* 2014; **513**: 214–218.
10 Baugher BWH, Churchill HOH, Yang YF, Jarillo-Herrero P. Optoelectronic devices based on electrically tunable p-n diodes in a monolayer dichalcogenide. *Nat Nanotechnol* 2014; **9**: 262–267.
11 Mak KF, McGill KL, Park J, McEuen PL. The valley Hall effect in MoS_2 transistors. *Science* 2014; **344**: 1489–1492.
12 He KL, Kumar N, Zhang L, Wang ZF, Mak KF *et al*. Tight bound excitons in monolayer WSe_2. *Phys Rev Lett* 2014; **113**: 026803.
13 Chernikov A, Berkelbach TC, Hill HM, Rigosi A, Li Y *et al*. Exciton binding energy and nonhydrogenic Rydberg series in monolayer WS_2. *Phys Rev Lett* 2014; **113**: 076802.
14 Zhu BR, Chen X, Cui XD. Exciton binding energy of monolayer WS_2. *Sci Rep* 2015; **5**: 9218.
15 Lin YX, Ling X, Yu LL, Huang SX, Hsu AL *et al*. Dielectric screening of excitons and trions in single-layer MoS_2. *Nano Lett* 2014; **14**: 5569–5576.
16 Ye Y, Wong ZJ, Lu XF, Zhu HY, Chen XH *et al*. Monolayer excitonic laser. 2015; arXiv:1503.06141.
17 Wang G, Marie X, Gerber I, Amand T, Lagarde D *et al*. Giant enhancement of the optical second-harmonic emission of WSe_2 monolayers by laser excitation at exciton resonances. *Phys Rev Lett* 2015; **114**: 097403.
18 Seyler KL, Schaibley JR, Gong P, Rivera P, Jones AM *et al*. Electrical control of second-harmonic generation in a WSe_2 monolayer transistor. *Nat Nanotechnol* 2015; **10**: 407–411.
19 Behnia K. Condensed-matter physics: polarized light boosts valleytronics. *Nat Nanotechnol* 2012; **7**: 488–489.
20 Zaslow B, Zandler ME. Two-dimensional analog to the hydrogen atom. *Am J Phys* 1967; **35**: 1118–1119.
21 Qiu DY, da Jornada FH, Louie SG. Optical spectrum of MoS_2: many-body effects and diversity of exciton states. *Phys Rev Lett* 2013; **111**: 216805.
22 Simon HJ, Bloembergen N. Second-harmonic light generation in crystals with natural optical activity. *Phys Rev* 1968; **171**: 1104–1114.
23 Bloembergen N. Conservation laws in nonlinear optics. *J Opt Soc Am* 1980; **70**: 1429–1436.
24 Boyd RW. Nonlinear Optics. Burlington, MA: Academic Press; 2008.
25 Kioseoglou G, Hanbicki AT, Currie M, Friedman AL, Gunlycke D *et al*. Valley polarization and intervalley scattering in monolayer MoS_2. *Appl Phys Lett* 2012; **101**: 221907.
26 Snoke DW, Rühle WW, Köhler K, Ploog K. Spin flip of excitons in GaAs quantum wells. *Phys Rev B* 1997; 55: 13789–13794.
27 Lakowicz JR. Topics in Fluorescence Spectroscopy Ch. 3. New York: Kluwer Academic Publishers; 2002.
28 Hong XP, Kim J, Shi SF, Zhang Y, Jin CH *et al*. Ultrafast charge transfer in atomically thin MoS_2/WS_2 heterostructures. *Nat Nanotechnol* 2014; **9**: 682–686.
29 Shi HY, Yan RS, Bertolazzi S, Brivio J, Gao B *et al*. Exciton dynamics in suspended monolayer and few-layer MoS_2 2D crystals. *ACS Nano* 2013; **7**: 1072–1080.
30 Kumar N, Cui QN, Ceballos F, He DW, Wang YS *et al*. Exciton-exciton annihilation in $MoSe_2$ monolayers. *Phys Rev B* 2014; **89**: 125427.
31 Yu T, Wu MW. Valley depolarization due to intervalley and intravalley electron-hole exchange interactions in monolayer MoS_2. *Phys Rev B* 2014; **89**: 205303.
32 Slavcheva G, Kavokin AV. Polarization selection rules in exciton-based terahertz lasers. *Phys Rev B* 2013; **88**: 085321.
33 Fleischhauer M, Imamoglu A, Marangos JP. Electromagnetically induced transparency: optics in coherent media. *Rev Mod Phys* 2005; **77**: 633.
34 Silberberg Y. Quantum coherent control for nonlinear spectroscopy and microscopy. *Annu Rev Phys Chem* 2009; **60**: 277–292.

This work is licensed under a Creative Commons Attribution-NonCommercial-NoDerivs 4.0 Unported License. The images or other third party material in this article are included in the article's Creative Commons license, unless indicated otherwise in the credit line; if the material is not included under the Creative Commons license, users will need to obtain permission from the license holder to reproduce the material. To view a copy of this license, visit http://creativecommons.org/licenses/by-nc-nd/4.0/

Supplementary information for this article can be found on the *Light Science and Applications*' website (http://www.nature.com/lsa/).